

# Thermoelectric transport properties of electron doped pyrite FeS<sub>2</sub>

Anustup Mukherjee and Alaska Subedi

CPHT, CNRS, École Polytechnique, Institut Polytechnique de Paris, 91128 Palaiseau, France

(Dated: November 13, 2023)

Pyrite FeS<sub>2</sub> has been investigated for a wide range of applications, including thermoelectrics due to previous observation of large thermopower at room-temperature. However, the values of thermopower reported in the literature is extremely sensitive to the nature of sample—whether they are natural or lab grown, bulk crystals or thin films—and an ambiguity in the magnitude and sign of thermopower of pure FeS<sub>2</sub> exists. Variation in the magnitude of room-temperature thermopower has also been observed in Co-doped samples. Therefore, it is of interest to clarify the intrinsic thermopower of this system that could be measured in more pure samples. In this paper, we investigate the thermoelectric properties of Co-doped FeS<sub>2</sub> using first principles calculations. We apply three different doping schemes to understand the effect of electron doping in FeS<sub>2</sub>, namely explicit Co-substitution, jellium doping and electron addition within rigid band approximation (RBA) picture. The calculated thermopower is less than  $-50 \mu\text{V/K}$  for all values of Co doping that we studied, suggesting that this system may not be useful in thermoelectric applications. Interestingly, we find that RBA substantially overestimates the magnitude of calculated thermopower compared to the explicit Co-substitution and jellium doping schemes. The overestimation occurs because the changes in the electronic structure due to doping-induced structural modification and charge screening is not taken into account by the rigid shift of the Fermi level within RBA. RBA is frequently used in first principles investigations of the thermopower of doped semiconductors, and Co-substituted FeS<sub>2</sub> illustrates a case where it fails.

## I. INTRODUCTION

Pyrite FeS<sub>2</sub> is a semiconductor with an indirect band gap of 0.95 eV [1, 2]. It is composed of earth-abundant elements that are nontoxic. Hence, it has been studied as an energy material for various applications, including photovoltaics [3–5], battery cathodes [6] and thermoelectrics [7–9]. Thermoelectricity is an important property that affects the efficiency of these functionalities, and the thermoelectric properties of natural and synthetic bulk FeS<sub>2</sub> crystals, as well as thin films, have been experimentally investigated extensively [8–13].

Studies made in the first half of the twentieth century reported a wide range of values and different signs for the Seebeck ( $S$ ) coefficient at room temperature, with  $S$  ranging from  $-115$  to  $524 \mu\text{V/K}$  [10]. Experimental work performed since then find similar divergence in the reported values of  $S$ , likely due to difficulty in controlling impurities and vacancies in this material that give it a finite carrier concentration. Measurements on natural n-type FeS<sub>2</sub> by Kato *et al.* report  $S$  of  $-300 \mu\text{V/K}$  at room temperature [8], while Karguppikar and Vedeshwar find absolute  $S$  ranging between  $120$ – $430$  and  $430$ – $660 \mu\text{V/K}$  for natural n- and p-type samples, respectively [11]. Experiments on lab-grown single crystals by Willeke *et al.* find  $S$  up to  $-320 \mu\text{V/K}$  for high-mobility samples that are n-type as determined from Hall measurements [14]. However, contradictory results are observed for their low-mobility sample, where the Seebeck coefficient is negative with a value of  $S = -11 \mu\text{V/K}$  while the measured Hall coefficient exhibits a positive value. Harada grew polycrystalline FeS<sub>2</sub> samples and observed room-temperature  $S$  of  $50 \mu\text{V/K}$  and a positive Hall coefficient [12]. Uhlig *et al.* and Rehman *et al.* also find their lab-grown poly-

crystalline sample to be p-type with room-temperature  $S$  of  $128$  and  $88 \mu\text{V/K}$ , respectively [9, 15]. Experiments on thin films all report positive  $S$  in the range  $60$ – $75 \mu\text{V/K}$  but both negative and positive sign of the Hall coefficient [16–19]. A recent study by Xi *et al.* on FeS<sub>2</sub> single crystals and thin films seems to resolve the above discrepancies by thermopower and Hall effect measurements [20]. They report that highest mobility crystals and thin films are always n-type, whereas a crossover to p-type behavior occurs as mobility decreases.

Doped FeS<sub>2</sub> has also been investigated to see if it exhibits improved transport properties, and Co doping has garnered interest as it lies next to Fe in the periodic table [21, 22]. Thomas *et al.* observed room-temperature  $S$  of  $-37 \mu\text{V/K}$  in their Co-annealed polycrystalline samples [23], whereas Uhlig *et al.* measured  $S = -60 \mu\text{V/K}$  in nanograins with Co concentration of 5% [9]. Díaz-Chao *et al.* grew FeS<sub>2</sub> thin films with inhomogeneous Co concentration of 8–39% that exhibited  $S$  up to  $-70 \mu\text{V/K}$  [24], while Clamagirand *et al.*'s thin films with 16% Co concentration showed room-temperature  $S$  of  $-40 \mu\text{V/K}$  [13].

The wide range of values for  $S$  reported for self- and Co-doped FeS<sub>2</sub> raises two questions: i) what are the actual values of  $S$  for various doping levels?, and ii) can  $S$  be optimized by Co doping? Density functional theory calculations can be useful in answering them because  $S$  in a large part depends on the details of the electronic structure of the material. Gudelli *et al.* and Harran *et al.* have calculated  $S$  using semi-classical Boltzmann transport theory and found optimized  $S$  in excess of  $-400 \mu\text{V/K}$  [25, 26]. However, these studies took account of doping by a rigid shift of the Fermi level, and the effects of elemental substitution and additional charge screening was not explicitly considered. In a recent work on

$\text{Co}_{1-x}\text{Fe}_x\text{S}_2$ , we showed that explicit substitution of Co by Fe changes both the broadening of the bands and their relative splitting in a way that is not described by the rigid band approximation [27]. Therefore, a more detailed study of the role of chemical doping on the thermoelectric properties of this system is warranted.

In this paper, we investigate how three different doping schemes, namely explicit Co substitution, jellium doping and electron addition within the RBA picture, affect the thermoelectric properties of pyrite  $\text{FeS}_2$ . We find that the three doping schemes give similar trends for  $S$  as a function of temperature, but the magnitude of  $S$  within the RBA is substantially larger than when explicit Co or jellium doping is considered. To rationalize this behavior, we analyzed the electronic structure and found that the Fermi level is at a steeper region of the density of states in the RBA but gets situated around a broader area upon Co substitution or jellium doping. The calculated room-temperature  $S$  for doping level equivalent to 25% Co is  $-46.71$ ,  $-19.67$ , and  $-14.68$   $\mu\text{V/K}$  within the RBA, Co substitution and jellium doping, respectively. We find that the magnitude of  $S$  remains below 50  $\mu\text{V/K}$  for all values of doping that we considered. Since good thermoelectrics generally have  $S$  in excess of 200  $\mu\text{V/K}$ , our results suggest that doped  $\text{FeS}_2$  is unlikely to exhibit good thermoelectric performance.

## II. COMPUTATIONAL DETAILS

First principles calculations were performed under the framework of density functional theory [28, 29] using the Vienna *Ab initio* Simulation package [30–32]. The exchange-correlation interaction was approximated by the local density approximation (LDA), and the projector augmented wave (PAW) [33] method was used. A converged energy cut-off of at least 420 eV and a  $\Gamma$ -centered  $k$ -point mesh of at least  $8 \times 8 \times 8$  were taken for the self-consistent cycles. The energy convergence criterion for these self-consistency cycles was set to  $10^{-8}$  eV. A  $k$ -point of mesh of at least  $24 \times 24 \times 24$  was used for the density of states (DOS) calculations. The valence electronic configurations of the pseudopotentials were  $3d^8 4s^1$  (Co),  $3d^7 4s^1$  (Fe) and  $3s^2 3p^4$  (S).

The RBA scheme was implemented by performing a shift of the Fermi energy in the electronic structure of  $\text{FeS}_2$  to incorporate additional electrons/unit cell corresponding to the equivalent Co doping values. In the jellium doping scheme, we explicitly added electrons as background charge in the unit cell of  $\text{FeS}_2$  and performed electronic structure calculations. For the explicit Co substitution case, successive replacement of Fe atoms by Co atoms were carried out.

The transport properties were calculated by solving the linearized Boltzmann transport equation (BTE) under the constant relaxation time approximation (CRTA) using the BoltzTraP2 code [34] with an interpolation factor of at least 60. Within the linearized Boltzmann transport

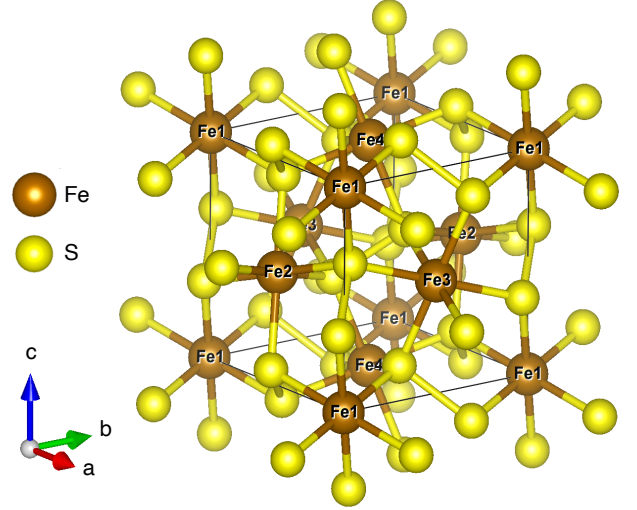


FIG. 1. The unit cell of pyrite  $\text{FeS}_2$  belonging to the space group  $Pa\bar{3}$ . The yellow-brown nearest-neighbour Fe-S bonds illustrates the octahedral coordination of the Fe atoms and the S-S dimer bonds are shown by solid yellow lines. The Fe atoms are marked by numbers. Sequential substitution of Fe1 and Fe2 by Co atoms leads to  $\text{Fe}_{0.75}\text{Co}_{0.25}\text{S}_2$  and  $\text{Fe}_{0.5}\text{Co}_{0.5}\text{S}_2$  corresponding to  $x = 0.75$  and  $0.5$ , respectively.

theory, the transport tensors are formulated as

$$\sigma_{\alpha\beta}(\mu, T) = \frac{1}{\Omega} \int \sigma_{\alpha\beta}(\epsilon) [-\partial_\epsilon f_\mu(\epsilon)] d\epsilon, \quad (1)$$

$$\nu_{\alpha\beta}(\mu, T) = \frac{1}{eT\Omega} \int \sigma_{\alpha\beta}(\epsilon) (\epsilon - \mu) [-\partial_\epsilon f_\mu(\epsilon)] d\epsilon, \quad (2)$$

$$\sigma_{\alpha\beta\gamma}(\mu, T) = \frac{1}{e^2 T \Omega} \int \sigma_{\alpha\beta\gamma}(\epsilon) (\epsilon - \mu)^2 [-\partial_\epsilon f_\mu(\epsilon)] d\epsilon, \quad (3)$$

where  $\Omega$  is the unit cell volume,  $e$  is the electron charge,  $f$  is the Fermi-Dirac distribution function,  $\mu$  is the chemical potential, and  $\epsilon$  is the band energy. The energy projected conductivity tensors are given by

$$\sigma_{\alpha\beta}(\epsilon) = \frac{1}{N} \sum_{i,\mathbf{k}} e^2 \tau v_\alpha(i, \mathbf{k}) v_\beta(i, \mathbf{k}) \delta(\epsilon - \epsilon_{i,\mathbf{k}}) \quad (4)$$

and similarly for  $\sigma_{\alpha\beta\gamma}$ . Here,  $\tau$  is the scattering time, and  $v_\alpha(i, \mathbf{k})$  is the group velocity  $\nabla_{\mathbf{k}} \epsilon_{i,\mathbf{k}}$  of the band  $i$  at the wave vector  $\mathbf{k}$ . The Seebeck and Hall coefficients are then expressed as

$$S(\mu, T) = \frac{\nu_{\alpha j}}{\sigma_{\alpha i}}, \quad (5)$$

$$R_H(\mu, T) = \frac{\nu_{\alpha\beta k}}{\sigma_{\alpha j} \sigma_{i\beta}}. \quad (6)$$

The factor  $(\epsilon - \mu)$  in Eq. 2 depends on the electronic structure of the system and captures the details of the particle-hole symmetry. The temperature dependence of the above transport properties comes from the derivative of the Fermi function  $-\partial_\epsilon f_\mu(\epsilon)$ . The scattering time  $\tau$  gets cancelled within CRTA for  $S$ . In the calculation of  $R_H$ , we used  $\tau \approx 10^{-14}$  s.

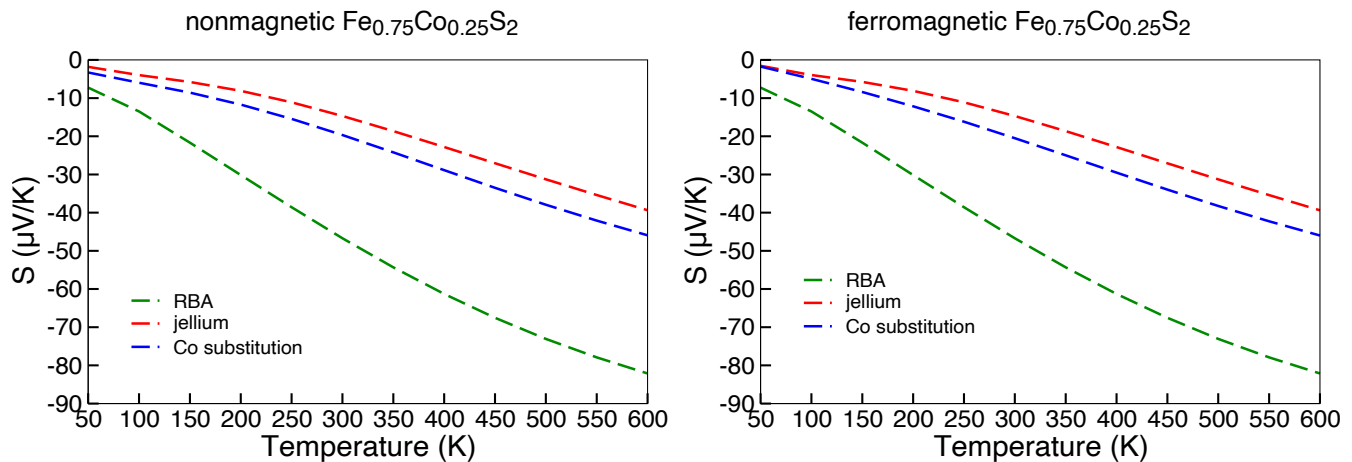


FIG. 2. Seebeck coefficient of the composition equivalent to  $\text{Fe}_{0.75}\text{Co}_{0.25}\text{S}_2$  ( $x = 0.75$ ) using RBA, jellium doping and explicit Co substitution within LDA. The left and the right columns show the results for the nonmagnetic and ferromagnetic phases, respectively.

### III. STRUCTURAL DETAILS

The pyrite form of  $\text{FeS}_2$ , belonging to the space group  $Pa\bar{3}$ , has four Fe atoms at  $4a$  (0,0,0) and eight S atoms at  $8c$  ( $u, u, u$ ), including their respective symmetry equivalent positions within the unit cell. The Fe atoms are coordinated with six S atoms, forming a corner-shared octahedra, whereas each S atom forms a S-S dimer shared by three octahedra. The unit cell of this phase of  $\text{FeS}_2$  is shown in Fig. 1. All the bond distances in this structure are controlled by the sole internal parameter of the system  $u$ .

We obtain  $\text{Fe}_{0.75}\text{Co}_{0.25}\text{S}_2$  by substituting a Co atom at the site labelled Fe1 in Fig. 1 and  $\text{Fe}_{0.5}\text{Co}_{0.5}\text{S}_2$  by additional substitution of a Co atom at the site Fe2. For the mixed Co/Fe compounds, experimental observation suggests that the lattice constants follow the Vegard's law [35, 36], which we utilize in our study. The internal parameter  $u$  controlling the different bond distances is found to be 0.3821 for  $\text{FeS}_2$  after relaxations that minimize the atomic forces. Due to symmetry reduction resulting from Co-substitution in the mixed compounds, there are multiple Co/Fe-S and S-S bond distances. Hence, they cannot be parameterized by a single  $u$  value. We have relaxed the atomic positions for the mixed compounds and the different bond distances thus obtained are reported in our recent study [27]. Within the different doping schemes, we have used the lattice parameter of  $\text{FeS}_2$  ( $x = 1$ ) for the RBA case. For jellium doped compounds, the lattice parameter of their electronically equivalent  $\text{Fe}_x\text{Co}_{1-x}\text{S}_2$  counterparts from Vegard's law were used, but the internal atomic positions were relaxed.

### IV. RESULTS AND DISCUSSIONS

We first consider the case where 25% of Fe are replaced by Co, which is the smallest doping level that can be simultaneously studied using RBA, jellium doping, and explicit Co substitution in a unit cell that contains four formula units. The temperature-dependent  $S$  obtained using these three schemes are shown in the left column of Fig. 2 for the nonmagnetic case. Our calculations reveal a similar behavior in  $S$  for all three doping schemes. Its sign remains negative while the magnitude increases with temperature. This indicates that electrons are the majority charge carriers and shows that bipolar conduction plays a minor role even at high temperature. However, we find that the thermopower within RBA is considerably higher than both the jellium doped and Co-substituted cases throughout the investigated temperature range despite having the same electron count. The calculated room-temperature values for  $S$  are  $-46.71$ ,  $-14.68$ ,  $-19.67$   $\mu\text{V/K}$ , respectively, for the RBA, jellium doped, and Co-substituted cases in the nonmagnetic phase. The corresponding calculated room temperature Hall numbers, which can be different from the chemical carrier concentration due to the nonparabolicity of the bands, are given in Table. I.

TABLE I. Room temperature Hall coefficient ( $R_H$ ) of  $\text{Fe}_{0.75}\text{Co}_{0.25}\text{S}_2$  using RBA, jellium doping and Co substitution within LDA.

Doping scheme	$R_H$ ( $10^{-10}$ m <sup>3</sup> /C)	$R_H$ ( $10^{-10}$ m <sup>3</sup> /C)
	nonmagnetic	ferromagnetic
RBA	-8.417	-8.417
jellium	-8.956	-8.957
Co substitution	-4.911	-5.135

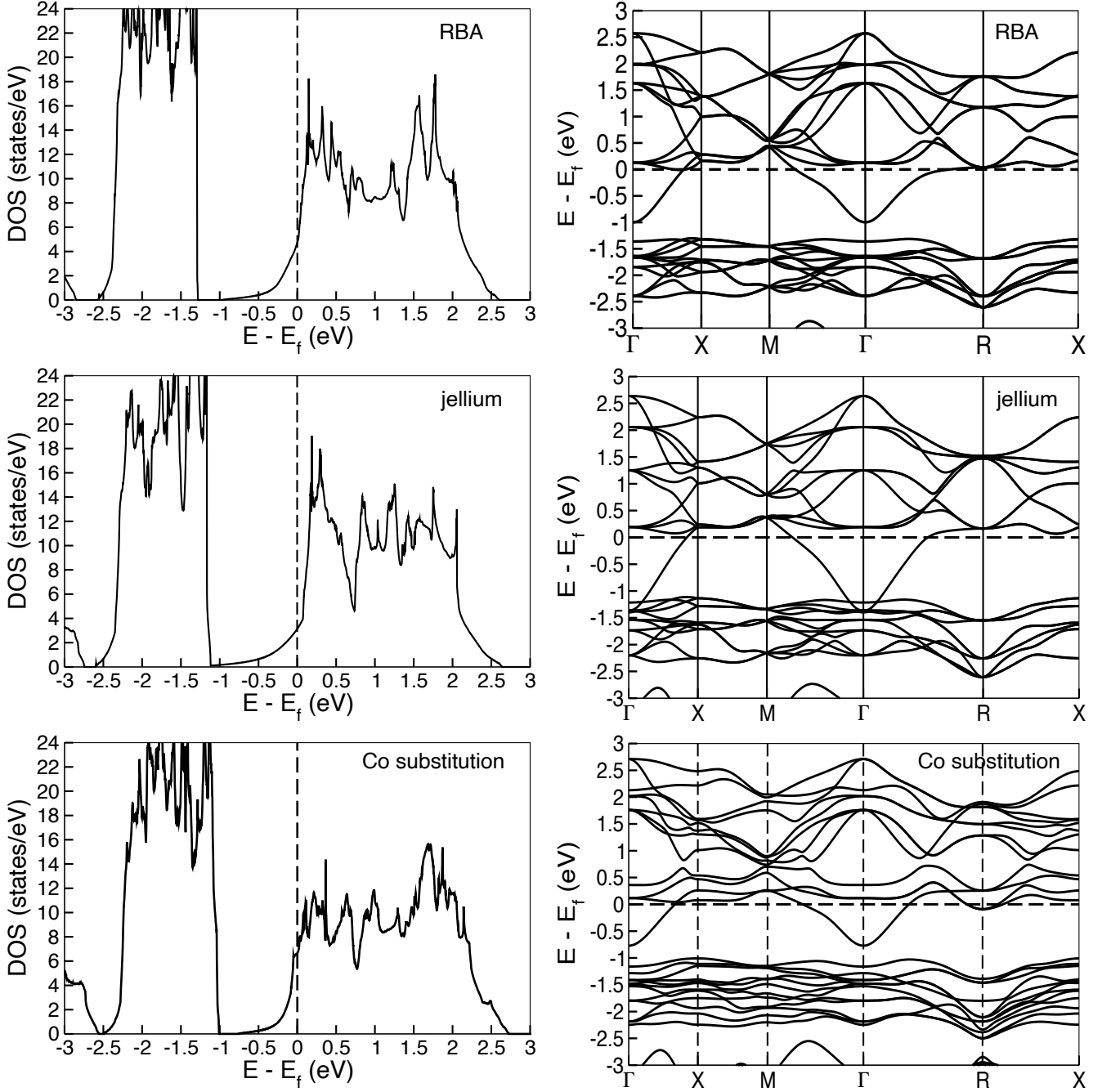


FIG. 3. Nonmagnetic total density of states (left) and band structures (right) of  $\text{Fe}_{0.75}\text{Co}_{0.25}\text{S}_2$  using RBA, jellium doping and explicit Co substitution within LDA. For the electronic structure in the RBA scheme, the Fermi energy is set to an electronic carrier concentration of  $6.32 \times 10^{21} \text{ cm}^{-3}$  corresponding to one additional electron/unit cell.

Experiments show that  $\text{Fe}_x\text{Co}_{1-x}\text{S}_2$  is ferromagnetic for  $x \geq 0.1$  [37, 38], and calculations that take into account this magnetic ordering should be considered for comparison against the experimental data below  $T_c$ . The right panel of Fig. 2 shows the calculated  $S$  of  $\text{Fe}_{0.75}\text{Co}_{0.25}\text{S}_2$  in the ferromagnetic phase for the three doping schemes, and the results are similar to the one obtained for the nonmagnetic cases. The room-temperature

$S$  within RBA remains  $-46.71 \mu\text{V/K}$ , while those obtained using jellium doping and explicit Co substitution are  $-14.69$  and  $-20.49 \mu\text{V/K}$ , respectively. The room-temperature  $S$  value for the jellium doped case is similar in both the states, whereas  $S$  observed for ferromagnetic Co-substituted case is a bit larger than that obtained for the nonmagnetic case.

To understand why RBA overestimates  $S$  compared to



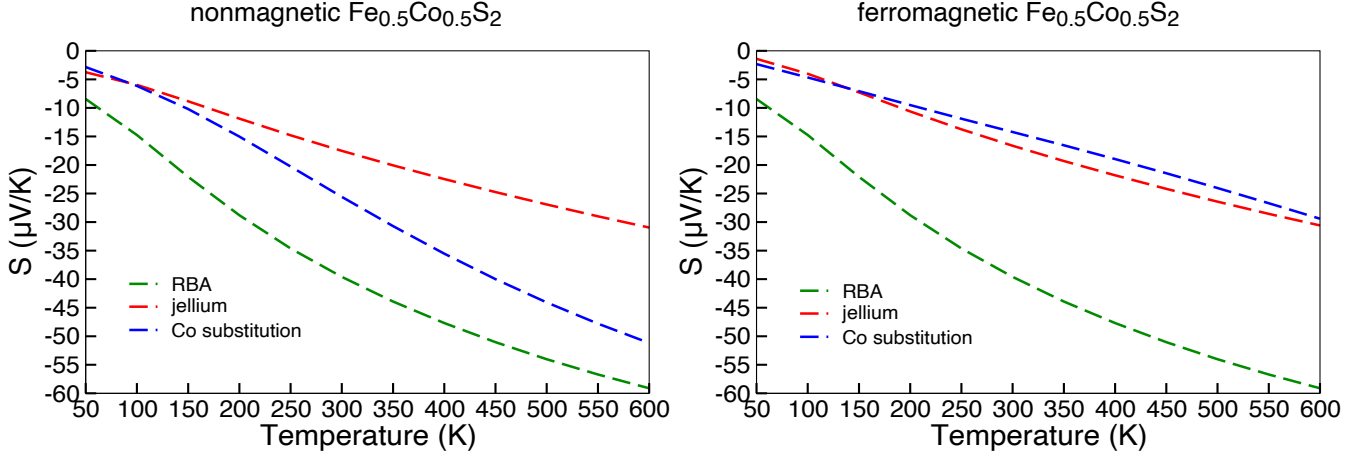


FIG. 4. Seebeck coefficient of the composition equivalent to  $\text{Fe}_{0.5}\text{Co}_{0.5}\text{S}_2$  using RBA, jellium doping and explicit Co substitution within LDA. The left and the right columns show the results for the nonmagnetic and ferromagnetic phases, respectively.

the more realistic jellium doping and explicit Co substitution schemes, we investigated the electronic structure near the Fermi level for the composition equivalent to  $\text{Fe}_{0.75}\text{Co}_{0.25}\text{S}_2$  using the three schemes. The resulting electronic density of states (DOS) and band structures are shown in the left and right columns of Fig. 3, respectively. In the case of RBA, the Fermi level is situated at a steep position in the DOS. The corresponding band structure shows that this is the result of a flat part of a band crossing the Fermi level near the  $R$  point. This band broadens and the flat part shifts above the Fermi level in the jellium-doped case. In the case of Co substitution, the narrow band shifts above the Fermi level because another dispersive conduction band at  $R$  dips below the Fermi level. Hence, the DOS at the Fermi level  $N(E_F)$  is situated in a less steep part in both the jellium doping and explicit Co substitution schemes. Since  $S \propto d \ln N(E_F)/dE$ , the steeper DOS near the Fermi level in the RBA case leads to a larger  $S$  compared to the jellium doping and explicit Co substitution cases.

The left and right panels of Fig. 4 show the calculated  $S$  for doping level equivalent to  $\text{Fe}_{0.5}\text{Co}_{0.5}\text{S}_2$  using the three schemes for the nonmagnetic and ferromagnetic phases, respectively. Again,  $S$  at room temperature is relatively small, with values of  $-39.60$ ,  $-17.52$ ,  $-25.58$   $\mu\text{V/K}$ , respectively, for the RBA, jellium doping, and Co substitution schemes in the nonmagnetic phase. Compared to the respective value obtained for  $\text{Fe}_{0.75}\text{Co}_{0.25}\text{S}_2$ ,  $S$  decreases for RBA, as one would expect from moving away from the band edge. However, the value for the explicit Co substitution case increases noticeably, while that for the jellium doping shows only a modest increase.

We investigated the DOS and band structure near the Fermi level of  $\text{Fe}_{0.50}\text{Co}_{0.50}\text{S}_2$  within the RBA, jellium doping and Co substitution schemes in the nonmagnetic phase, which are shown in the left and right columns of Fig. 5, respectively, to understand the differences in the electronic structure that result in different values of  $S$

within these three doping schemes. The Fermi energy is located at a steep region of the DOS within RBA and leads to a larger  $S$  compared to jellium doping and Co substitution schemes. The Fermi energy gets shifted to the broader shoulder of the peak in the jellium doped case, whereas it is located inside a valley in the explicit Co substitution case. By looking at the structure of the DOS near the Fermi level, it is surprising that the  $S$  in explicit Co-substituted case is larger than the jellium doped case. The respective band structures in the right column of Fig. 5 shows the presence of flat bands crossing the Fermi level around  $\Gamma$  and along  $R$ - $X$  in the explicit Co-substituted case, and this may be the cause of the larger  $S$  compared to the values obtained for the jellium doped case at room and higher temperatures. In the ferromagnetic case (not shown), the Fermi level is still situated in a steep region in the RBA case, but it is located in a relatively broader region in the jellium doped and explicit Co-substituted cases. This again results in a larger value of  $S$  for the RBA case compared to the latter two schemes. Interestingly, the presence of ferromagnetism reduces the unevenness in the DOS near the Fermi level of the explicit Co-substituted case, which reduces the  $S$  compared to the respective value calculated for the nonmagnetic case.

Finally, we calculated the thermopower at lower electron concentrations of 1, 5, 10 and 15% using the RBA and jellium doping schemes in the nonmagnetic phase, which is shown in Fig. 6. For these doping values, the explicit Co substitution scheme is not feasible using the four-formula unit conventional unit cell that we have used. Interestingly, both the RBA and jellium doping yield similar calculated values for  $S$  near room temperature at a doping level of 5%. However, calculations at larger doping levels of 10 and 15% again show the tendency of RBA to overestimate  $S$  discussed above. The room temperature  $S$  values for these doping levels are reported in Table. II, and they show that the calculated

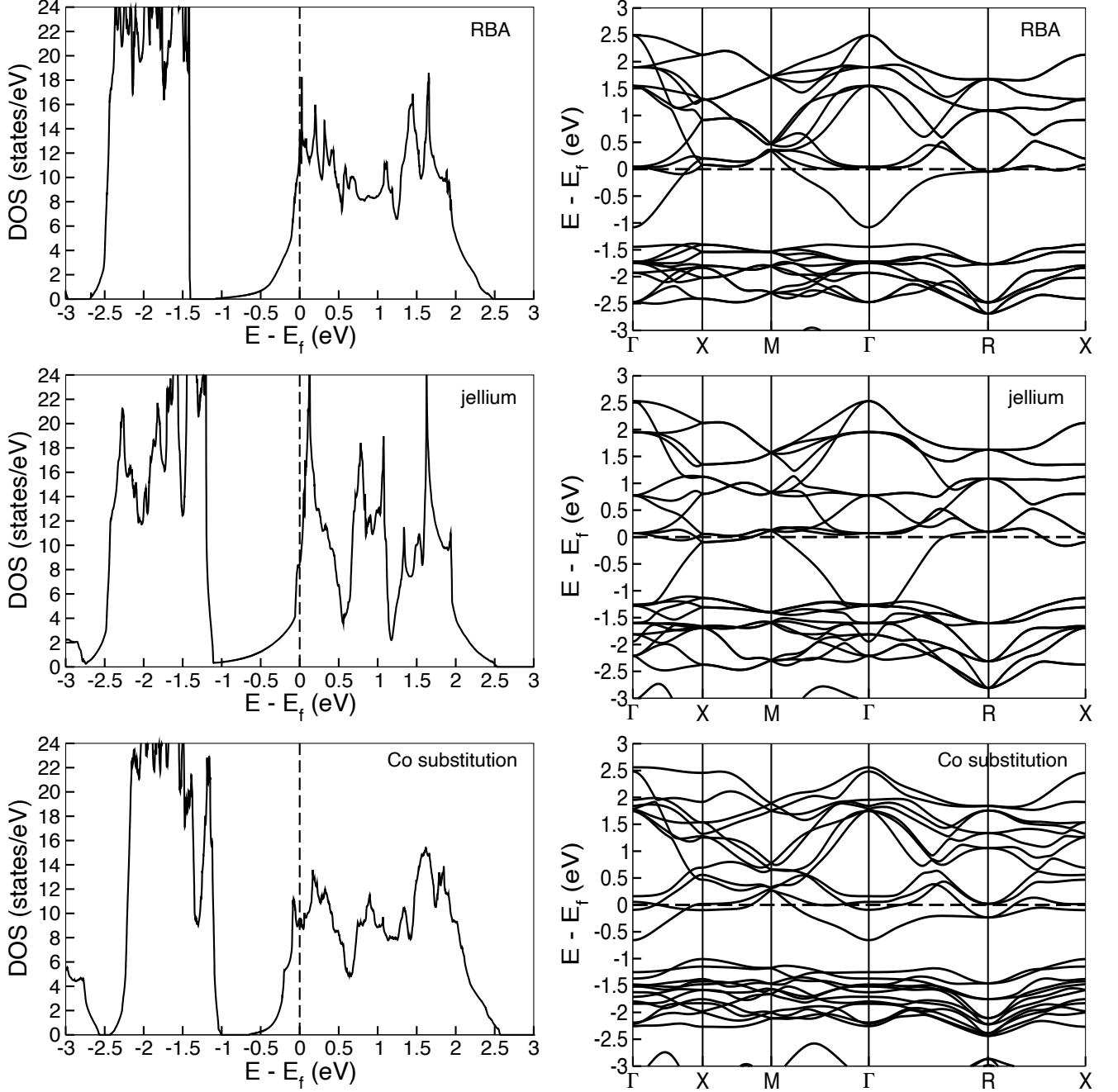


FIG. 5. Nonmagnetic total density of states (left) and band structures (right) of  $\text{Fe}_{0.5}\text{Co}_{0.5}\text{S}_2$  ( $x = 0.5$ ) using RBA, jellium doping and explicit Co substitution within LDA. For the electronic structure in the RBA scheme, the Fermi energy is set to an electronic carrier concentration of  $1.26 \times 10^{22} \text{ cm}^{-3}$  corresponding to two additional electrons/unit cell.

$S$  is negative and the room-temperature value remains below  $50 \mu\text{V/K}$  even for the lowest doping value.

## V. CONCLUSIONS

We have investigated the thermoelectric properties of electron doped  $\text{FeS}_2$  using three different schemes,

namely the RBA, jellium doping and explicit Co substitution. This was motivated by the wide range of values experimentally reported for the Seebeck coefficient at room temperature for this system. We studied doping levels up to 50% Co substitution of Fe and considered both the nonmagnetic and ferromagnetic phases. The sign of  $S$  is negative and its magnitude is relatively small ( $< 50 \mu\text{V/K}$ ) for all the doping schemes and levels that

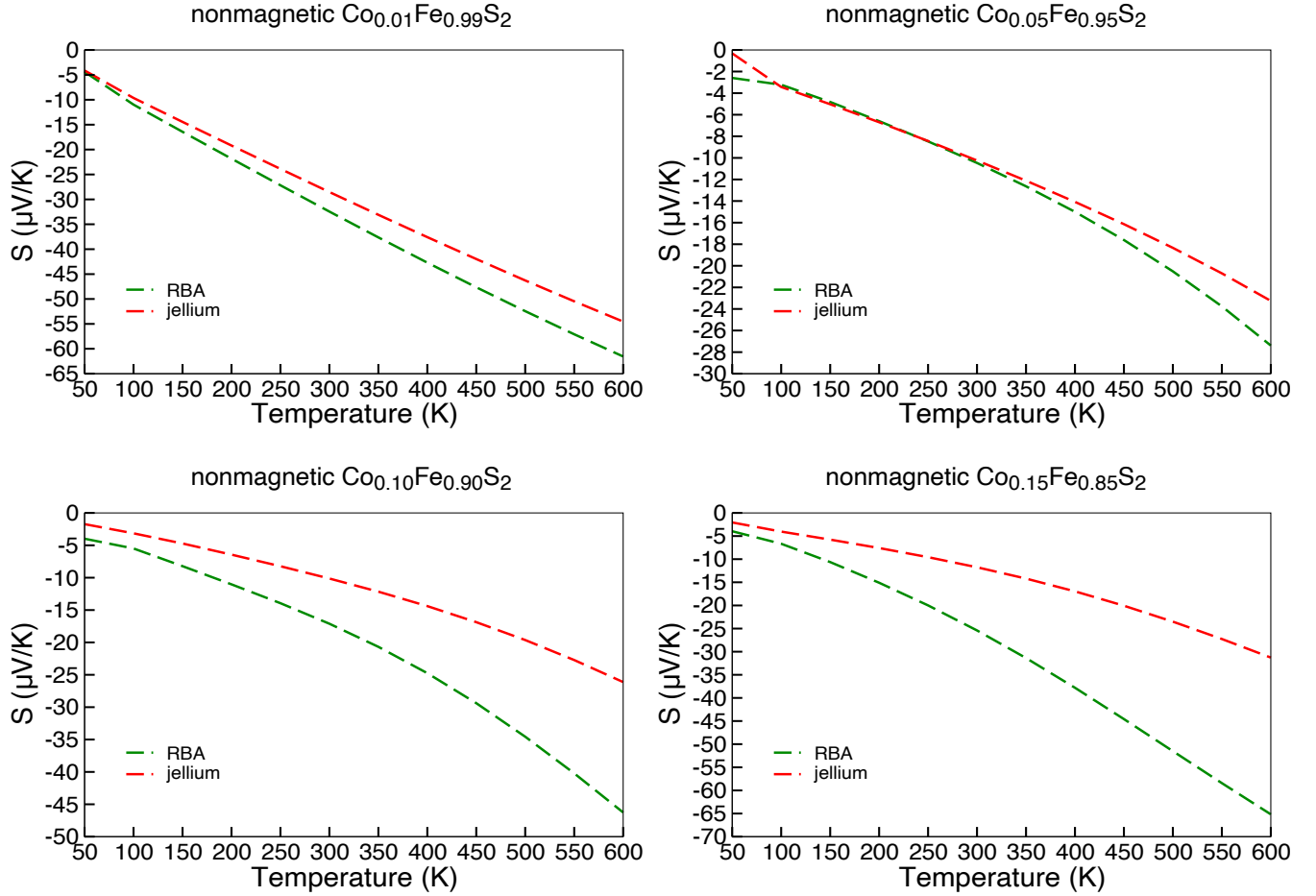


FIG. 6. Seebeck coefficient of  $\text{Fe}_x\text{Co}_{1-x}\text{S}_2$  corresponding to  $x = 1, 5, 10$  and  $15\%$  doping concentrations using RBA and jellium doping schemes within LDA in the nonmagnetic phase.

TABLE II. Nonmagnetic room-temperature thermopower ( $S$ ) for 1, 5, 10, 15, 20 and 25% doping levels within RBA and jellium doping schemes using LDA.

Composition	$S$ ( $\mu\text{V/K}$ )	
	RBA	jellium
$\text{Fe}_{0.99}\text{Co}_{0.01}\text{S}_2$	-32.45	-28.52
$\text{Fe}_{0.95}\text{Co}_{0.05}\text{S}_2$	-10.47	-10.24
$\text{Fe}_{0.90}\text{Co}_{0.10}\text{S}_2$	-17.11	-10.13
$\text{Fe}_{0.85}\text{Co}_{0.15}\text{S}_2$	-25.41	-11.75
$\text{Fe}_{0.75}\text{Co}_{0.25}\text{S}_2$	-46.71	-14.68
$\text{Fe}_{0.50}\text{Co}_{0.50}\text{S}_2$	-39.60	-17.52

we considered. The RBA overestimates  $S$  compared to the jellium doping and explicit Co substitution schemes, which we rationalized by observing that the DOS near

the Fermi level is steeper within the RBA. Neither of the three doping schemes exactly described the real samples that are studied in the experiments. However, they should reasonably approximate the various ways the electronic structure changes due to electron doping. In particular, jellium doping takes into account the changes in carrier concentration in a homogeneous way, while explicit Co substitution considers the role of inhomogeneity. The fact that the calculated  $S$  is relatively low irrespective of the concentration level and doping scheme considered suggests that electron doped  $\text{FeS}_2$  may not be a good thermoelectric material.

## ACKNOWLEDGMENTS

We express our gratitude to Sylvie Hébert for useful discussions. This work was supported by Agence Nationale de la Recherche under grant ANR-21-CE50-0033 and GENCI-TGCC under grant A0130913028.

- [1] A. Schlegel and P. Wachter, Optical properties, phonons and electronic structure of iron pyrite  $\text{FeS}_2$ , *Journal of Physics C: Solid State Physics* **9**, 3363 (1976).
- [2] A. Ennaoui, S. Fiechter, H. Goslowsky, and H. Tributsch, Photoactive synthetic polycrystalline pyrite  $\text{FeS}_2$ , *Journal of The Electrochemical Society* **132**, 1579 (1985).
- [3] A. Ennaoui, S. Fiechter, C. Pettenkofer, N. Alonso-Vante, K. Büker, M. Bronold, C. Höpfner, and H. Tributsch, Iron disulfide for solar energy conversion, *Sol. Energy Mater. Sol. Cells* **29**, 289 (1993).
- [4] Y. Tamm, R. Schieck, K. Ellmer, and S. Fiechter, Growth mechanism and electronic properties of doped pyrite  $\text{FeS}_2$  crystals, *J. Crystal Growth* **146**, 271 (1995), vapour Growth and Epitaxy 1994.
- [5] V. Eyert, K.-H. Höck, S. Fiechter, and H. Tributsch, Electronic structure of  $\text{FeS}_2$ : The crucial role of electron-lattice interaction, *Phys. Rev. B* **57**, 6350 (1998).
- [6] E. Strauss, D. Golodnitsky, and E. Peled, Study of phase changes during 500 full cycles of Li/composite polymer electrolyte/ $\text{FeS}_2$  battery, *Electrochim. Acta* **45**, 1519 (2000).
- [7] H. Banerjee, N. Godhaunkar, and U. Pal, Upgradation and studies on semiconducting properties of pyrite ( $\text{FeS}_2$ ) for device applications, *Materials Letters* **10**, 99 (1990).
- [8] K. Kato, Y. Okamoto, J. Morimoto, and T. Miyakawa, The thermoelectric properties of  $\text{FeS}_2$ , *J. Mater. Sci. Lett.* **16**, 914 (1997).
- [9] C. Uhlig, E. Guenes, A. S. Schulze, M. T. Elm, P. J. Klar, and S. Schlecht, Nanoscale  $\text{FeS}_2$  (pyrite) as a sustainable thermoelectric material, *J. Electron. Mater.* **43**, 2362 (2014).
- [10] M. Telkes, Thermoelectric power and electrical resistivity of minerals, *American Mineralogist* **35**, 536 (1950).
- [11] A. M. Karguppikar and A. G. Vedeshwar, Electrical and optical properties of natural iron pyrite  $\text{FeS}_2$ , *Phys. Stat. Sol. (a)* **109**, 549 (1988).
- [12] T. Harada, Transport properties of iron dichalcogenides  $\text{FeX}_2$  ( $X = \text{S}, \text{Se}$  and  $\text{Te}$ ), *J. Phys. Soc. Japan* **67**, 1352 (1998).
- [13] J. Clamagirand, J. Ares, E. Flores, P. Diaz-Chao, F. Leardini, I. Ferrer, and C. Sánchez, Influence of temperature on thermoelectric properties of  $\text{Fe}_x\text{Co}_{1-x}\text{S}_2$  thin films: A semiconductor to semimetal conversion, *Thin Solid Films* **600**, 19 (2016).
- [14] G. Willeke, O. Blenk, C. Kloc, and E. Bucher, Preparation and electrical transport properties of pyrite  $\text{FeS}_2$  single crystals, *J. Alloys Compd.* **178**, 181 (1992).
- [15] U. Rehman, J. Jacob, K. Mahmood, A. Ali, A. Ashfaq, M. Basit, N. Amin, S. Ikram, S. Hussain, H. Noor, A. ul Ahmad, and N. ur Rehman, Improving the thermoelectric performance of hydrothermally synthesized  $\text{FeS}_2$  nanoparticles by post sulfurization, *Ceramics International* **46**, 20496 (2020).
- [16] B. Thomas, T. Cibik, C. Höpfner, K. Diesner, G. Ehlers, S. Fiechter, and K. Ellmer, Formation of secondary iron-sulphur phases during the growth of polycrystalline iron pyrite  $\text{FeS}_2$  thin films by MOCVD, *Journal of Materials Science: Materials in Electronics* **9**, 61 (1998).
- [17] J. R. Ares, M. León, N. M. Arozamena, J. Sánchez-Páramo, P. Celis, I. J. Ferrer, and C. Sánchez, Evolution of the seebeck coefficient during the formation and crystallization of pyrite thin films, *Journal of Physics: Condensed Matter* **10**, 4281 (1998).
- [18] L. Reijnen, B. Meester, A. Goossens, and J. Schoonman, In situ mass spectrometric study of pyrite ( $\text{FeS}_2$ ) thin film deposition with metallorganic chemical vapor deposition, *Journal of The Electrochemical Society* **147**, 1803 (2000).
- [19] J. Ares, I. Ferrer, and C. Sánchez, Majority carriers in pyrite thin films: an analysis based on seebeck and hall coefficient measurements, *Thin Solid Films* **431-432**, 511 (2003).
- [20] X. Zhang, M. Li, J. Walter, L. O'Brien, M. A. Manno, B. Voigt, F. Mork, S. V. Baryshev, J. Kakalios, E. S. Aydil, and C. Leighton, Potential resolution to the doping puzzle in iron pyrite: Carrier type determination by hall effect and thermopower, *Phys. Rev. Mater.* **1**, 015402 (2017).
- [21] S. Lehner, K. Savage, and J. Ayers, Vapor growth and characterization of pyrite  $\text{FeS}_2$  doped with Co, Ni, and As: Variations in semiconducting properties, *J. Cryst. Growth* **286**, 306 (2006).
- [22] S. Guo, D. P. Young, R. T. Macaluso, D. A. Browne, N. L. Henderson, J. Y. Chan, L. L. Henry, and J. F. DiTusa, Charge transport in cobalt-doped iron pyrite, *Phys. Rev. B* **81**, 144424 (2010).
- [23] B. Thomas, K. Ellmer, W. Böhne, J. Röhrich, M. Kunst, and H. Tributsch, Photoeffects in cobalt doped pyrite  $\text{FeS}_2$  films, *Solid State Commun.* **111**, 235 (1999).
- [24] P. Díaz-Chao, I. Ferrer, and C. Sánchez, Co distribution through n-type pyrite thin films, *Thin Solid Films* **516**, 7116 (2008).
- [25] V. K. Gudelli, V. Kanchana, S. Appalakondaiah, G. Vaitheeswaran, and M. C. Valsakumar, Phase stability and thermoelectric properties of the mineral  $\text{FeS}_2$ : An ab initio study, *J. Phys. Chem. C* **117**, 21120 (2013).
- [26] I. Harran, Y. Li, H. Wang, Y. Chen, and Y. Ni, Iron disulfide compound: a promising thermoelectric material, *Materials Research Express* **4**, 105907 (2017).
- [27] A. Mukherjee and A. Subedi, Minority-spin conducting states in Fe substituted pyrite  $\text{CoS}_2$ , *J. Phys.: Condens. Matter* **36**, 025501 (2023).
- [28] P. Hohenberg and W. Kohn, Inhomogeneous electron gas, *Phys. Rev.* **136**, B864 (1964).
- [29] W. Kohn and L. J. Sham, Self-consistent equations including exchange and correlation effects, *Phys. Rev.* **140**, A1133 (1965).
- [30] G. Kresse and J. Hafner, Ab initio molecular dynamics for liquid metals, *Phys. Rev. B* **47**, 558 (1993).
- [31] G. Kresse and J. Furthmüller, Efficiency of ab-initio total energy calculations for metals and semiconductors using a plane-wave basis set, *Comput. Mat. Sci.* **6**, 15 (1996).
- [32] G. Kresse and J. Furthmüller, Efficient iterative schemes for ab initio total-energy calculations using a plane-wave basis set, *Phys. Rev. B* **54**, 11169 (1996).
- [33] G. Kresse and D. Joubert, From ultrasoft pseudopotentials to the projector augmented-wave method, *Phys. Rev. B* **59**, 1758 (1999).
- [34] G. K. Madsen, J. Carrete, and M. J. Verstraete, BoltzTraP2, a program for interpolating band structures and calculating semi-classical transport coefficients, *Comput. Phys. Commun.* **231**, 140 (2018).



- [35] L. Wang, K. Umemoto, R. M. Wentzcovitch, T. Y. Chen, C. L. Chien, J. G. Checkelsky, J. C. Eckert, E. D. Dahlberg, and C. Leighton,  $\text{Co}_{1-x}\text{Fe}_x\text{S}_2$ : A tunable source of highly spin-polarized electrons, [\*Phys. Rev. Lett.\* \*\*94\*\*, 056602 \(2005\)](#).
- [36] S. F. Cheng, G. T. Woods, K. Bussmann, I. I. Mazin, R. J. Soulen, E. E. Carpenter, B. N. Das, and P. Lubitz, Growth and magnetic properties of single crystal  $\text{Fe}_{1-x}\text{Co}_x\text{S}_2$  ( $x = 0.35 - 1$ ), [\*J. Appl. Phys.\* \*\*93\*\*, 6847 \(2003\)](#).
- [37] H. S. Jarrett, W. H. Cloud, R. J. Bouchard, S. R. Butler, C. G. Frederick, and J. L. Gillson, Evidence for itinerant  $d$ -electron ferromagnetism, [\*Phys. Rev. Lett.\* \*\*21\*\*, 617 \(1968\)](#).
- [38] S. Guo, D. P. Young, R. T. Macaluso, D. A. Browne, N. L. Henderson, J. Y. Chan, L. L. Henry, and J. F. DiTusa, Discovery of the griffiths phase in the itinerant magnetic semiconductor  $\text{Fe}_{1-x}\text{Co}_x\text{S}_2$ , [\*Phys. Rev. Lett.\* \*\*100\*\*, 017209 \(2008\)](#).